Rare bioparticle detection *via* deep metric learning

Shaobo Luo,[af] Yuzhi Shi,[b] Lip Ket Chin, [ID][bd] Yi Zhang,[c] Bihan Wen,[b] Ying Sun,[f] Binh T. T. Nguyen,[b] Giovanni Chierchia,[a] Hugues Talbot,[e] Tarik Bourouina, [ID] *[a] Xudong Jiang*[b] and Ai-Qun Liu [ID] *[bg]

Recent deep neural networks have shown superb performance in analyzing bioimages for disease diagnosis and bioparticle classification. Conventional deep neural networks use simple classifiers such as SoftMax to obtain highly accurate results. However, they have limitations in many practical applications that require both low false alarm rate and high recovery rate, *e.g.*, rare bioparticle detection, in which the representative image data is hard to collect, the training data is imbalanced, and the input images in inference time could be different from the training images. Deep metric learning offers a better generatability by using distance information to model the similarity of the images and learning function maps from image pixels to a latent space, playing a vital role in rare object detection. In this paper, we propose a robust model based on a deep metric neural network for rare bioparticle (*Cryptosporidium* or *Giardia*) detection in drinking water. Experimental results showed that the deep metric neural network achieved a high accuracy of 99.86% in classification, 98.89% in precision rate, 99.16% in recall rate and zero false alarm rate. The reported model empowers imaging flow cytometry with capabilities of biomedical diagnosis, environmental monitoring, and other biosensing applications.

1. Introduction

Rare bioparticle detection is essential to various applications such as cancer diagnosis and prognosis, viral infections, and implementing early warning systems in water monitoring.[1–6] In these applications, the target bioparticles in the sample are extremely rare with a huge abundance of background particles. For example, the ratio of the target bioparticle and background bioparticles could be 1 in 1000 (0.1%) or even less.[7] Currently, bioimage analysis has made a huge progress, benefitting from rich-dataset supervised learning using deep neural networks.[4,5,8] However, conventional deep neural networks only use simple classifiers such as SoftMax to obtain highly accurate results with the confidence that the deep neural network learns more distinct features than traditional machine learning in classification. Thus, they sometimes get unexpected results in many practical

applications, *e.g.*, rare bioparticle detection[7,9–11] and bioparticle sorting[8,12,13] because it is hard to collect representative image data in those applications and the input images in inference time may be distinct from those during training. These applications also require the model to have a performance of low false alarm as well as high recovery rate in practical environments. For example, a large amount of false alarms will introduce high-cost consequential actions.[14] Up to now, it remains a great challenge in the detection of rare bioparticles in practical applications.

Conventional deep neural networks use simple classifier to make the decision of seen/unseen classes. Therefore, they often make wrong predictions, and do so confidently.[15–18] For example, the conventional deep neural network model predicts wrongly (it predicts the pollutants as *Cryptosporidium* or *Giardia*) with a high confidence level (>99.99%) as shown in Fig. 1. These inaccuracies arise from the conventional classification

[a]ESYCOM, CNRS UMR 9007, Universite Gustave Eiffel, ESIEE Paris, Noisy-le-Grand 93162, France. E-mail: tarik.bourouina@esiee.fr

[b]School of Electrical & Electronic Engineering, Nanyang Technological University, 639798, Singapore. E-mail: EXDJiang@ntu.edu.sg; EAQLiu@ntu.edu.sg

[c]School of Mechanical & Aerospace Engineering, Nanyang Technological University, 639798, Singapore

[d]Center for Systems Biology, Massachusetts General Hospital, Massachusetts 02114, USA

[e]CentraleSupelec, Universite Paris-Saclay, Saint-Aubin 91190, France

[f]Institute for Infocomm Research (I2R), Agency for Science, Technology and Research (A*STAR), 138668, Singapore

[g]Nanyang Environment and Water Research Institute, Nanyang Technological University, 637141, Singapore
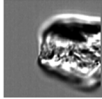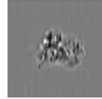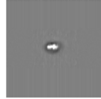
Pollution				
Detection Result	*Giardia*	*Giardia*	*Giardia*	*Cryptosporidium*
Confidence Level	0.99999	0.99999	0.99673	0.99988

Fig. 1 Wrong prediction in conventional deep neural networks. Conventional deep neural networks often make wrong predictions and do so confidently when the images are not seen in the training process. The pollutions are predicted as targets, *Giardia* or *Cryptosporidium*, with a confidence level >99.99%.

approaches such as convolutional neural networks (CNNs) with a linear Softmax classifier[11] (Fig. 2(a)) that limit their ability to detect novel examples.[9,15,17,19,20] As a result, conventional Softmax-based approaches are not suitable for open-set rare bioparticle detection. For example, a highly accurate algorithm based on a sophisticated densely connected neural network for bioparticle classification was developed for rare bioparticle detection,[8] but it only achieved a sensitivity and specificity of 77.3% and 99.5%, respectively.

Deep metric learning[10] in Fig. 2(b) provides a possible direction to improve open-set detection by learning a map from the input image space to an output embedding features in the latent space. Instead of using the SoftMax classifier, this approach uses semantic similarity such as the Euclidean distance to constrain the models. It does not rely on the cross-entropy loss but proposes another class of network loss, *i.e.*, the contrastive loss. Thus, the sum of the output class probabilities is not doom to be one and this provides it a generatability.[9] Generative model is essentially a metric learning problem whereby the key is to learn a large margin distance metric within the latent space when the testing data are usually disjoint from the training dataset.

Unsupervised deep metric learning is used to learn a low-dimensional subspace and preserve useful geometrical information of the samples. On the other hand, supervised deep metric learning is used to learn a projection from the sample space to the feature space and measure the Euclidean metric in this feature space to discriminate the results. The metric learning is defined to study a map function f with a dataset $\chi = \{x, y, z, \ldots\}$, whereby $f: \chi \to \mathbb{R}^n$ is well defined mapping and $d: \mathbb{R}^n \times \mathbb{R}^n \to \mathbb{R}_+$ is the Euclidean distance over $\mathbb{R}^n$. $d_f(x, y) = d(f(x), f(y)) = \|f(x) - f(y)\|_2$ is close to zero when x and y are similar.

The mathematical definition of Euclidean distance $d(x, y)$ between x and y is expressed as[10]

$$d(x, y) = \|f(x) - f(y)\|_2 = \sqrt[2]{(f(x) - f(y))^T (f(x) - f(y))} \quad (1)$$

where $x, y \in \chi$, and it is assumed that metric $d(x, y): \chi \times \chi \to \mathbb{R}_+$ satisfies the following properties as

$$d(x, y) \geq 0 \quad (2a)$$

$$d(x, y) = d(y, x) \quad (2b)$$

$$d(x, z) \leq d(x, y) + d(y, z) \quad (2c)$$

$$d(x, x) = 0 \quad (2d)$$

Deep metric learning is widely applied in signature verification,[21] face verification and recognition,[22] and person re-identification.[23]

In this paper, a rare bioparticle detection system is demonstrated (Fig. 3), which consists of an imaging flow cytometry system to capture the images of all pollutants and create an image database. A deep neural network based on deep metric learning and a decision algorithm are designed to detect rare bioparticles of *Cryptosporidium* and *Giardia*. The model leverages convolutional neural network to study the rich features in the dataset and learning distinct metric by using Siamese network[21] and contrastive loss, which maximizes the distance of different classes and minimizes the distance of similar classes. Experimental results showed that the deep metric learning studies good features and performs better than conventional deep learning, which was manifested to be a solid network model for rare bioparticle detection problems.
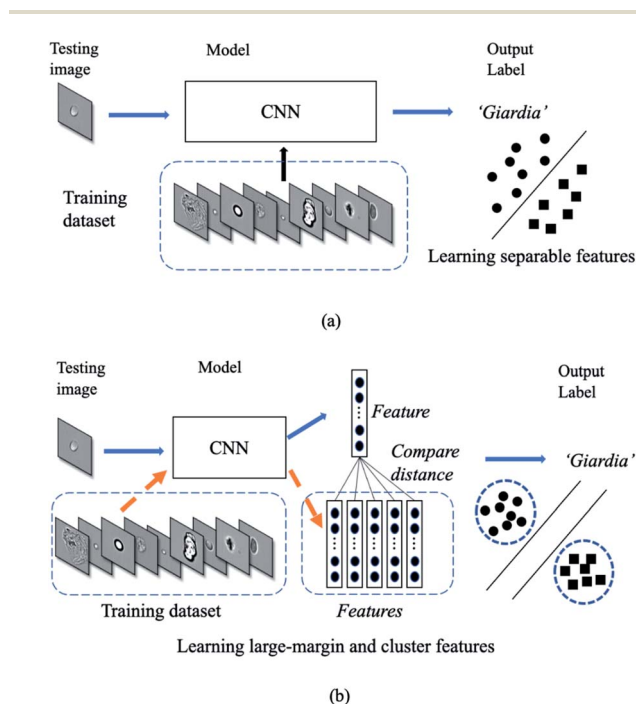

Fig. 2 Deep classification *vs.* deep metric learning. (a) In deep classification, the model only studies a boundary. (b) In deep metric learning, the model studies a more generative representation with similar classes are close and the unsimilar classes are far away.

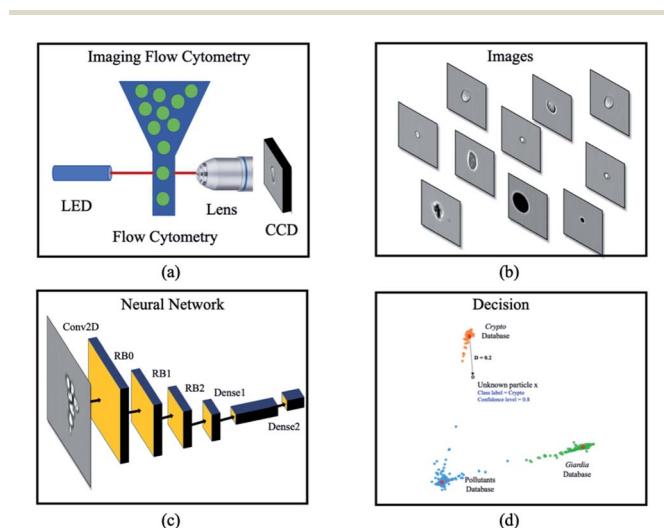Fig. 3 Overview of a deep metric neural network for rare bioparticle detection using an imaging flow cytometry. Water sample is processed using (a) the imaging flow cytometry system (Amnis® ImageStream®X Mk II), capturing the images of all pollutants and creating (b) an image database. (c) Deep metric neural network, and (d) decision algorithms are used for classification and detection.

2. Methods and materials

2.1 Bioparticle profiling

First, the samples were imaged using the imaging flow cytometry (Amnis® ImageStream®X Mk II). Bioparticles such as *Cryptosporidium*, *Giardia*, microplastics and other pollutants such as dirt and cell debris with size ranging from 3 to 14 μm that naturally exist in drinking water were included in the study. The naturally existing pollutants were obtained by concentrating 10 litres of drinking water using a water filtration system. Formalin-treated *Cryptosporidium* oocysts, *Giardia* cysts (Waterborne™ Inc.) and synthetic microplastic beads (Thermo Fisher Scientific, Duke Scientific and Polysciences Inc.) of different sizes (1.54 μm, 3 μm, 4 μm, 4.6 μm, 5 μm, 5.64 μm, 8 μm, 10 μm, 12 μm and 15 μm) were spiked separately in 200 μL water. Bioparticles were hydrodynamically focused by a sheath flow and flowed through the detection region with phosphate buffered saline solution (PBS) used as the sheath medium. Single bioparticles were illuminated with an LED light source, and brightfield images (Fig. 4) were acquired with a charge-coupled device (CCD) camera[24] using a 60× objective in Fig. 3(a).

2.2 Bioparticle image dataset

The raw image sequence files (.RIF) of different samples were captured. The raw brightfield images were extracted from the image sequence files by IDEAS software (accompanying with the ImageStream) and patched to 120 × 120 pixels as in Fig. 3(b). From millions of acquired raw images, 89 663 images were selected to construct the dataset by experts. The image dataset consists of three classes: *Cryptosporidium* (2078 images), *Giardia* (3438 images), and natural pollutants and beads (84 147 images). The brightfield images of protozoa had complex patterns, such as distinct sizes, degree of aggregation and different internal structures, which complicated the learning task.

2.3 Deep metric learning for rare bioparticle detection

Siamese network[21] is the most popular deep metric learning network structure which is used to train the deep learning model shown in Fig. 5(a). The base network structure of deep
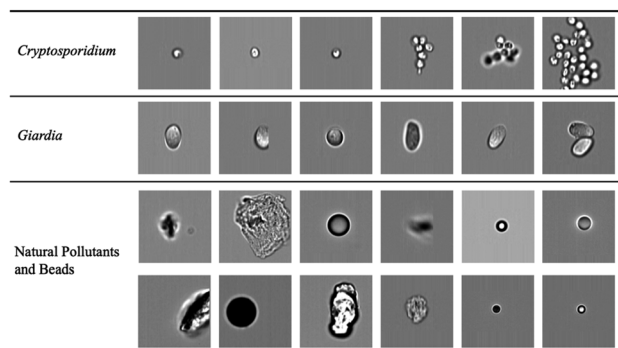

Fig. 4 Bioparticle image dataset. Each row represents one type of bioparticle. From the top to bottom are *Cryptosporidium*, *Giardia*, natural pollutants and beads. All subfigures share the same scale bar.
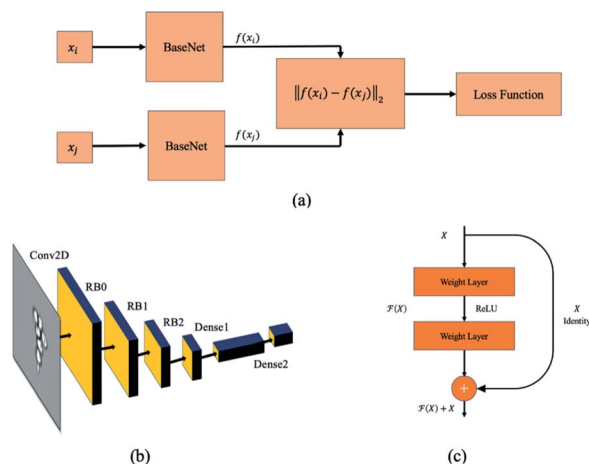

Fig. 5 Siamese network. (a) The structure of Siamese network for training deep metric learning. The twin networks share the same network parameters. A loss function is attached to this twin network to regularize the network. (b) Embedding network. (c) Residual block.

metric learning model is illustrated in Fig. 5(b). The input of embedding network is a grayscale image with 120 × 120 pixels and a convolutional layer with a filter size of 7 × 7 is used in the first stage. Then, three residual network blocks (RB0 to RB2)[25] are attached to the first convolution neural network layer. The output of the last residual network block RB2 is flattened, and then followed by a fully-connected layer[26] together with a parametric ReLU (PReLU) layer.[27] Finally, a fully-connected layer with 2 output units is attached to the PReLU layer to generate the latent feature vector of bioparticles. The detail parameters of the embedding network are listed in Table 1.

The first convolutional 2D layer (Conv2D in Fig. 5(b))[28] takes an $h \times w \times n$ input feature map X^i, where h is the spatial height, w is the spatial width and n is the output channels of the feature map (120 × 120 × 1). The input X^i is transformed into a $60 \times 60 \times 64$ output feature maps X^o and expressed as[29]

$$X^o_{x,y,z} = \delta \left(\sum_{i,j,k} F_{i,j,k,z} X^i_{x+i-1,y+j-1,k} + b_z \right) \qquad (3)$$

where $z = 1, 2, \ldots, m$ and $k = 1, 2, \ldots, n$. The input feature map X^i is convolved with a number of feature detectors, each of which has a three-dimensional filter F in the present layer (7 × 7 × 1), and a bias b. A ReLU function $\delta(x)$ is attached to this convolution operator.

Three cascaded residual network blocks (RB0 to RB2 in Fig. 5(b))[25] with down sampling (stride = (2, 2)) are attached to

Table 1 Network parameters of the embedding network

Layer/block	Type	Output dimension	Params
Conv2d	Convolution	60 × 60 × 64	9536
RB0	Residual block	30 × 30 × 64	147 968
RB1	Residual block	15 × 15 × 128	525 568
RB2	Residual block	8 × 8 × 256	2 099 712
Pool	Average pool	2 × 2 × 256	0
Dense1	Fully connected	256	262 400
PReLU	Parametric ReLU	256	1
Dense2	Fully connected	2	514

the first convolution layer. The RB has two 3×3 convolutional layers and the same number of output channels as shown in Fig. 5(c). In the end, a batch normalization layer and a ReLU activation function follow each convolutional layer. In addition, an identify path is added to connect the input to the output directly.

The classifier is implemented by two fully connected layers (dense layer in Fig. 5(b)). It takes the last output of RB2 as the input and applies cascaded matrix multiplications and non-linear function to the weight matrix $\textbf{\textit{F}}$ and bias $\textbf{\textit{b}}$ to produce a vector with two dimensions in the latent space. The equation of fully connected layer can be expressed as

$$X^{\textbf{o}} = \delta(\textbf{\textit{F}}X^{\textbf{i}} + \textbf{\textit{b}}) \tag{4}$$

The PReLU layer is used after the fully-connected layer, which is expressed as

$$f(x_i) = \begin{cases} x_i, & \text{if } x_i > 0 \\ a_i x_i, & \text{if } x_i \leq 0 \end{cases} \tag{5}$$

where x_i is the input value and a_i is the parameter of the PReLU layer.

2.4 Model training

The model is trained with Siamese network-based structure. Siamese network is proposed for the signature's verification in 1994 and used for training the neural network. The network consists of two base embedding networks and a joint output neuron. Residual network blocks are used as the embedding networks to extract the features. The two embedding networks share the same weights, and the identical sub-networks extract feature vectors from two images simultaneously and the joined neuron measures the distance between the two feature vectors in the latent space by using a metric. In the training process, the similar and dissimilar pairs (x_i and x_j) are passed through the network and generate features vector in the latent space named $f(x_i)$ and $f(x_j)$. In the loss function, the distance metric $d(x, y) = \|f(x) - f(y)\|_2$ is regressed to minimize the distance between the similar pairs and keep the distance of the dissimilar pairs. The contrastive loss is used to train the Siamese network. For the pair of input (x_i, x_j), it is a positive pair if x_i and x_j are semantically similar and negative pair if they are dissimilar. The training process of Siamese network deals with minimizing the contrastive loss, which is expressed as

$$L\left(\{W^{(m)}, b^{(m)}\}_{m=1}^{M}\right) = \sum_{(i,j) \in \mathscr{S}} h\left(d_f\left(\textbf{\textit{x}}_i, x_j\right) - \tau_1\right)^2 \\ + \sum_{(i,j) \in \mathscr{D}} h\left(\tau_2 - d_f\left(\textbf{\textit{x}}_i, x_j\right)\right)^2 \tag{6}$$

where $h(x) = \max(0, x)$ is the hinge loss function, and $\tau_1 = 0.9$ and $\tau_2 = 1.0$ are two positive thresholds with $\tau_1 < \tau_2$, respectively. $\mathscr{S} = \{(i,j)\}$ is the similar pair and $\mathscr{D} = \{(i,j)\}$ is the dissimilar pair.

The deep metric learning model is implemented with deep learning framework-PyTorch[30] and trained over an Ubuntu GPU server[31] with four Nvidia GeForce RTX 2080 cards and the Intel Xeon CPU E5-2650. To train and evaluate the performance of the model, the selected image dataset is randomly split into a training, validation and testing dataset with 48%, 12% and 40% of the total number of images, respectively. Later, the images in the training dataset are augmented to 10 000 images, and each image is randomly sampled from the dataset and processed by position transformation, horizontal and vertical flipping, rotation or zooming. The weight of the deep neural networks is initialized with the Glorot uniform initializer[32] at a mean value of zero and a standard deviation at 10^{-2}, and the network is trained in an end-to-end fashion using the Adam stochastic optimizing algorithm.[33] The parameters for Adam are $\beta_1 = 0.9$, $\beta_2 = 0.999$, and a learning rate decay is used for training. The positive or negative pair is generated on the fly. First, it enumerates current image anchor from the image list. Then, the positive image is randomly selected from rest images of the same class and the negative image is randomly selected from the images in rest classes. Early stop is also used to prevent overfitting by stopping the training when the model's performance on validation dataset start to degrade.[34] A maximum of 300 epochs is used to train the model.

2.5 Deep metric learning based classifier

The deep metric network studies a map from the images into a latent space and cannot be used directly to classify the images. In order to classify the rare bioparticle images with deep metric learning model, further processing is needed to be added in the end of this neural network model. It converts the values in the latent vector into a target class label and a confidence score. As shown in Fig. 6, the class label is assigned by the closed cluster center, which can be calculated by either mean latent vectors (mean center) or Gaussian Mixture Models (GMM)[35] of a known class, such as *Cryptosporidium*, in the training dataset. The confidence score is used to present the similarity between the
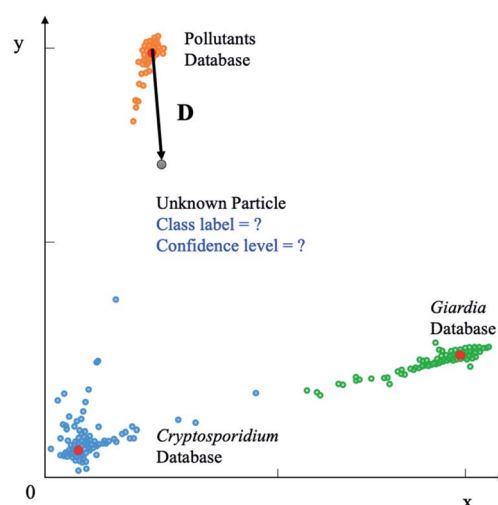

Fig. 6 Deep metric learning based classification. The unknown bioparticle is classified to correspond classes. Class label is assigned to classify the unknown particles by the closed cluster center (red). Confidence level is used to present the similarity of unknown particles to certain databased collected by *Cryptosporidium* and *Giardia* samples.

target bioparticle to the certain classes, which are collected in the training phase. The confidence score can be calculated by the distance of the target bioparticle to the center of certain class on the distribution diagram of the latent space or a Gaussian estimator.

Gaussian distribution[36] is a continuous probability distribution, which has a characteristic with symmetric "Bell curve" shape that quickly falls off toward 0. GMM is a probabilistic model, which assumes that the underlying data belong to a linear combination of several Gaussian distributions. A GMM model gives a posterior distribution over K Gaussian distributions, which shows better performance on optimizing model complexity.[37] The GMM can be represented by[38]

$$P\left(x|\pi,\mu,\sum\right)=\sum_{i=1}^{K}\pi_i\mathcal{N}\left(x|\mu_i,\sum_i\right) \tag{7}$$

where $\mathcal{N}(x|\mu,\sum)$ is a normal distribution, x is a multi-dimension vector variable, μ is the mean of this x and $\sum$ is the covariance matrix. The $\mathcal{N}(x|\mu,\sum)$ is given by[38]

$$\mathcal{N}\left(x|\mu,\sum\right)=\frac{1}{(2\pi)^{D/2}|\sum|^{1/2}}\exp\left(-\frac{1}{2}(x-\mu)^T\sum^{-1}(x-\mu)\right) \tag{8}$$

where D is the number of dimensions of the feature vector. The π_i are mixing coefficients. It satisfied $0\le\pi_i\le1$ and $\sum_{i=0}^{N}\pi_i=1$. With the assumption that x_i come from independent K mixture distributions insider C, the equation can be expressed as[38]

$$P\left(C|\pi,\mu,\sum\right)=\prod_{n=1}^{N}\sum_{i=1}^{K}\pi_i\mathcal{N}\left(x_n|\mu_i,\sum_i\right) \tag{9}$$

Expectation-maximization (EM) algorithm is used to find the local maximum likelihood and estimates of individual parameters in GMM (μ and $\sum$). EM is an iterative algorithm, which follows the rule that every iteration strictly increases the maximum likelihood. EM algorithm may not reach the global optimal point, but it can guarantee to local saddle point. The EM algorithm consists of two main steps: expectation and maximization. The expectation step calculates the expectation of the clusters when each $x_i\in X$ is assigned to the clusters with given $\mu,\sum,\pi$. The maximization step maximizes the expectation in previous step by find suitable parameters.

First, the program randomly assigned samples $X=\{x_1,x_2,\ldots,x_n\}$ to components estimated mean $\hat{\mu_1},\hat{\mu_2},\ldots,\hat{\mu_k}$. For example, $\hat{\mu_1}=x_6,\hat{\mu_2}=x_{20},\hat{\mu_3}=x_{21},\hat{\mu_4}=x_{33},\hat{\mu_5}=x_{60}$ when $N=100$ and $K=5$. Then, $\sum_1=\sum_2=\ldots=\sum_k=\text{Cov}(x)=E[(X-\overline{x})(X-\overline{x})^T]$ is assigned where $\overline{x}=E(X)$, and all mixing coefficients are set to a uniform distribution with $\hat{\pi}_1=\hat{\pi}_2=\ldots\hat{\pi}_k=\frac{1}{K}$. In the expectation step, $p(C_k|x_i,\hat{\pi}_k,\hat{\mu}_k,\hat{\Sigma}_k)$ is given by[38]

$$p\left(C_k|x_i,\hat{\pi}_k,\hat{\mu}_k,\hat{\Sigma}_k\right)=\frac{\hat{\pi}_k\mathcal{N}\left(\hat{x}_i\Big|\hat{\mu}_k,\hat{\Sigma}_k\right)}{\sum_{j=1}^{K}\hat{\pi}_j\mathcal{N}\left(x_i|\hat{\mu}_j,\hat{\Sigma}_j\right)} \tag{10}$$

In the maximization step, $(\hat{\pi}_k,\hat{\mu}_k,\hat{\Sigma}_k)^{(i+1)}=\underset{\hat{\pi}_k,\hat{\mu}_k,\hat{\Sigma}_k}{\text{argmax}}p(C_k|x_i,(\hat{\pi}_k,\hat{\mu}_k,\hat{\Sigma}_k)^i)$ and can be calculated as[38]

$$\hat{\pi}_k=\sum_{i=1}^{N}\frac{p\left(C_k|x_i,\hat{\pi}_k,\hat{\mu}_k,\hat{\Sigma}_k\right)}{N} \tag{11a}$$

$$\hat{\mu}_k=\frac{\sum_{i=1}^{N}p\left(C_k|x_i,\hat{\pi}_k,\hat{\mu}_k,\hat{\Sigma}_k\right)x_i}{\sum_{i=1}^{N}p\left(C_k|x_i,\hat{\pi}_k,\hat{\mu}_k,\hat{\Sigma}_k\right)} \tag{11b}$$

$$\hat{\Sigma}_k=\frac{\sum_{i=1}^{N}p\left(C_k|x_i,\hat{\pi}_k,\hat{\mu}_k,\hat{\Sigma}_k\right)\left(x_i-\hat{\mu}_k\right)\left(x_i-\hat{\mu}_k\right)^T}{\sum_{i=1}^{N}p\left(C_k|x_i,\hat{\pi}_k,\hat{\mu}_k,\hat{\Sigma}_k\right)} \tag{11c}$$

The whole EM process repeats iteratively until the EM algorithm converges to a point and gives a maximum likelihood estimate for each $\hat{\pi}_k,\hat{\mu}_k,\hat{\Sigma}_k$.
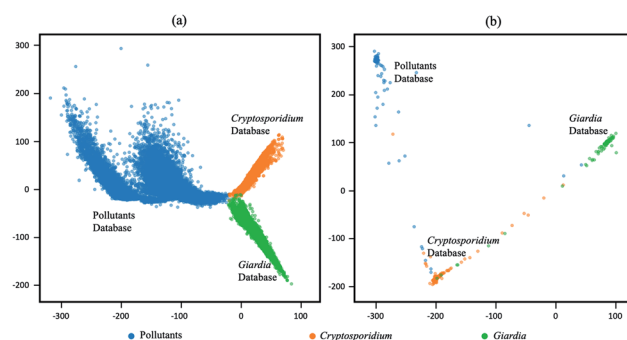

Fig. 7 Visualization on 2D latent space of conventional deep classification-based model and deep metric learning which mapped by embedding network. (a) Conventional deep classification-based model, (b) deep metric learning based model.
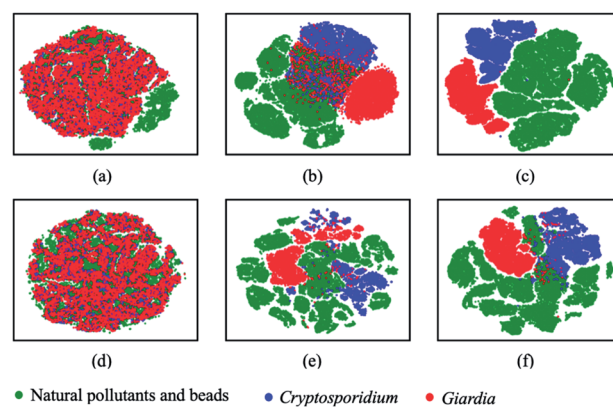

Fig. 8 Visual on intermediate layers with t-SNE on deep metric learning and conventional classification-based model. (a–c) The lower, middle, and high level of deep metric learning, (d–f) the lower, middle, and high level of conventional deep classification-based model.

Table 2 Precision, recall and F1 score on test dataset

Methods	Measurement (%)			
	Accuracy	Precision	Recall	F1 score
Deep classification	99.71	97.84	98.55	98.19
Deep metric learning	99.86	98.84	99.17	99.00

Table 3 Confusion matrix of conventional deep classification

Class		Prediction		
		Pollutants	*Cryptosporidium*	*Giardia*
Actual	Pollutants	**29 610**	35	14
	Cryptosporidium	20	**807**	4
	Giardia	10	8	**1357**

Table 4 Confusion matrix of deep metric learning-based classification

Class		Prediction		
		Pollutants	*Cryptosporidium*	*Giardia*
Actual	Pollutants	**29 639**	17	3
	Cryptosporidium	9	**820**	2
	Giardia	6	9	**1360**

3. Results and discussions

3.1 Classification evaluation

The output latent vectors of the deep metric neural network are mapped to a 2D latent space by embedding network as shown in Fig. 7. Compared with the conventional deep classification method in Fig. 7(a), the deep metric learning model is trained using the Siamese network in Fig. 7(b) and the contrastive loss shows better performance. The dots of the similar images in deep metric learning are closer and the dissimilar images are kept far away from others, providing the ability of generatability. Moreover, the t-SNE graphs of RB0 to RB2 from low level to high level features in Fig. 8 also show that the data is well separated in the deep metric learning based model in Fig. 8(a)–

(c) even in the shallow layers by comparing with the conventional classification-based method in Fig. 8(d)–(f).

For classification, the GMM model is selected because it can show how much confidence is associated to the target cluster, and it has the same accuracy of 99.86% with the mean center. The final results of the model comparison between deep metric learning and conventional deep classification are summarized in Table 2. The model based on deep metric learning is superior to the model based on conventional deep classification neural networks in terms of accuracy, precision, recall and F1 score. The model based on deep metric learning network achieves 99.86% in accuracy, 98.89% in precision rate, 99.16% in recall rate and 99.02% in F1 score. On the other hand, the model based on conventional deep classification gives 99.71% in accuracy, 97.84% in precision, 98.55% in recall and 98.19% in F1 score. The results in Tables 3 and 4 also show that the performance of the individual class in deep metric learn-based model is better when it has a large quantity of training data. For example, the classification result on contaminated particles is much better in deep metric learning.

3.2 Model verification using spiked samples

In order to evaluate the performance of the deep metric learning model on rare bioparticle detection in real situation, *Cryptosporidium* and *Giardia* were spiked into the concentrated water sample to simulate rare bioparticle in contaminated water. In total, ten testing were run and the captured images were detected by the software with a confidence level at 0.98 and verified by biological experts based on their morphologies. The final results are summarised in Table 5. The deep metric learning gives zero false warning signal, which is vital to implement the early warning system that needs the specificity of 100%. In comparison, the conventional deep classification gives false positive signal in test 1, 3, 5, 6, 7, 10, especially false warning signals in test 7 and 10 are not acceptable. Some confused images are listed in Fig. 9. The first row shows the false positive images detected from the background pollution. They are easy to be identified for human, but failure to be obtained in conventional deep neural network. The second row shows some examples that *Cryptosporidium* are classified to *Giardia* and *vice versa*. On the contrary, deep metric learning-based model serves as a paradigm to deal with the rare cell

Table 5 *Cryptosporidium* and *Giardia* detection using deep metric learning

No.	Spike	Image number	Manual counting	Sensitivity	Specificity	Alarm	Recovery rate
1	20C	23 483	7	85.7%	100%	Yes	85.7%
2	20C	18 422	8	75.0%	100%	Yes	75.0%
3	20C	21 834	10	80.0%	100%	Yes	80.0%
4	20G	19 383	7	100.0%	100%	Yes	100.0%
5	20G	18 320	9	88.9%	100%	Yes	88.9%
6	20G	24 872	6	83.3%	100%	Yes	88.3%
7	0	20 000	0	—	100%	No	—
8	0	20 000	0	—	100%	No	—
9	0	20 000	0	—	100%	No	—
10	0	20 000	0	—	100%	No	—
Mean				85.5%	100%	—	85.5%
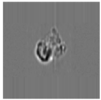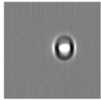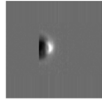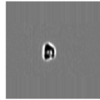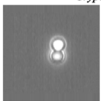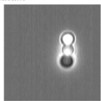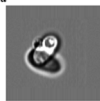
Pollution				
Detection Result	*Giardia*	*Giardia*	*Giardia*	*Cryptosporidium*
Confidence Level	0.98765	1.00000	0.70841	0.83984
	Cryptosporidium		*Giardia*	
Detection Result	*Giardia*	*Giardia*	*Cryptosporidium*	*Cryptosporidium*
Confidence Level	0.68781	0.99999	0.99673	0.99988

Fig. 9 Wrong prediction in conventional deep neural networks. The first row shows the false positive images detected from the background pollution. They are easy to be identified for human, but failure to be obtained in conventional deep neural network. The second row shows some examples that *Cryptosporidium* are classed to *Giardia* and *vice versa*.

detection. For the recovery rate, the deep metric learning gives an average of 85.5%.

4. Conclusions

Siamese-based deep metric learning provides a set of new tools for learning latent vectors by leveraging both convolutional neural network and deep metric learning. In this paper, we present a deep neural network based on deep metric learning for rare bioparticle detection by incorporating Siamese constraint in the learning process. The model can learn interpretable latent representation that preserves semantic structure of similar and dissimilar images. The experimental results demonstrate that Siamese-based deep metric learning can achieve classification-based accuracy while encoding more semantic structural information in the latent embedding. Thus, it is suitable for rare bioparticle detection, and achieves 99.86% in accuracy and zero false alarm. The model empowers intelligent imaging flow cytometry with the capability of rare bioparticle detection, benefiting the biomedical diagnosis, environmental monitoring, and other biosensing applications.

Author contributions

S. L., A. Q. L. and T. B. jointly conceived the idea. B. T. T. N. performed experiments. Y. Z., A. E., X. H. Z., B. H. W., G. C., H. T., Y. S., T. B., X. D. J. and A. Q. L. were involved in the discussion and data analysis. S. L., A. Q. L., Y. Z., X. D. J, L. K. C. and Y. Z. S. wrote the manuscript. T. B., X. D. J. and A. Q. L. supervised and coordinated all of the work.

Conflicts of interest

The authors declare no conflict of interest.

References

1 N. Meng, E. Lam, K. K. M. Tsia and H. K.-H. So, *IEEE J. Biomed. Health Inform.*, 2018, **23**, 2091–2098.
2 Z. Göröcs, M. Tamamitsu, V. Bianco, P. Wolf, S. Roy, K. Shindo, K. Yanny, Y. Wu, H. C. Koydemir and Y. Rivenson, *Light: Sci. Appl.*, 2018, **7**, 1–12.
3 Y. Wu, A. Calis, Y. Luo, C. Chen, M. Lutton, Y. Rivenson, X. Lin, H. C. Koydemir, Y. Zhang and H. Wang, *ACS Photonics*, 2018, **5**, 4617–4627.
4 G. Kim, Y. Jo, H. Cho, H.-s. Min and Y. Park, *Biosens. Bioelectron.*, 2019, **123**, 69–76.
5 A. Isozaki, H. Mikami, H. Tezuka, H. Matsumura, K. Huang, M. Akamine, K. Hiramatsu, T. Iino, T. Ito and H. Karakawa, *Lab Chip*, 2020, **20**, 2263–2273.
6 X. Mao and T. J. Huang, *Lab Chip*, 2012, **12**, 1412–1416.
7 Y. Chen, P. Li, P.-H. Huang, Y. Xie, J. D. Mai, L. Wang, N.-T. Nguyen and T. J. Huang, *Lab Chip*, 2014, **14**, 626–645.
8 Y. Zhang, M. Ouyang, A. Ray, T. Liu, J. Kong, B. Bai, D. Kim, A. Guziak, Y. Luo and A. Feizi, *Light: Sci. Appl.*, 2019, **8**, 1–15.
9 M. Masana, I. Ruiz, J. Serrat, J. van de Weijer and A. M. Lopez, 2018, arXiv preprint arXiv:1808.05492.
10 J. Lu, J. Hu and J. Zhou, *IEEE Signal Process. Mag.*, 2017, **34**, 76–84.
11 I. Goodfellow, Y. Bengio, A. Courville and Y. Bengio, *Deep learning*, MIT press Cambridge, 2016.
12 Y. Z. Shi, S. Xiong, Y. Zhang, L. K. Chin, Y. Y. Chen, J. B. Zhang, T. Zhang, W. Ser, A. Larrson and S. Lim, *Nat. Commun.*, 2018, **9**, 1–11.
13 Y. Shi, S. Xiong, L. K. Chin, J. Zhang, W. Ser, J. Wu, T. Chen, Z. Yang, Y. Hao and B. Liedberg, *Sci. Adv.*, 2018, **4**, eaao0773.
14 T. A. Reichardt, S. E. Bisson, R. W. Crocker and T. J. Kulp, Presented in Proc. SPIE 6945, *Optics and Photonics in Global Homeland Security IV*, 69450R, April 2008.
15 A. Bendale and T. Boult, *IEEE Comput. Soc. Conf. Comput. Vis. Pattern Recogn.*, 2015, 1893–1902.
16 M. A. Pimentel, D. A. Clifton, L. Clifton and L. Tarassenko, *Signal Process.*, 2014, **99**, 215–249.
17 A. Bendale and T. E. Boult, *IEEE Comput. Soc. Conf. Comput. Vis. Pattern Recogn.*, 2016, 1563–1572.
18 D. Hendrycks and K. Gimpel, 2016, arXiv preprint arXiv:1610.02136.
19 B. J. Meyer, B. Harwood and T. Drummond, *IEEE Int. Conf. Image Process.*, 2018, 151–155.
20 D. S. Trigueros, L. Meng and M. Hartnett, 2018, arXiv preprint arXiv:1811.00116.
21 J. Bromley, I. Guyon, Y. LeCun, E. Säckinger and R. Shah, *NIPS (News Physiol. Sci.)*, 1994, **6**, 737–744.

22 Y. Taigman, M. Yang, M. A. Ranzato and L. Wolf, *IEEE Comput. Soc. Conf. Comput. Vis. Pattern Recogn.*, 2014, 1701–1708.

23 R. R. Varior, M. Haloi and G. Wang, *ECCV*, 2016.

24 E. R. Fossum and D. B. Hondongwa, *IEEE J. Electron Devices Soc.*, 2014, **2**(3), 33–43.

25 K. He, X. Zhang, S. Ren and J. Sun, *IEEE Comput. Soc. Conf. Comput. Vis. Pattern Recogn.*, 2016, 770–778.

26 Y. LeCun, Y. Bengio and G. Hinton, *Nature*, 2015, **521**, 436–444.

27 K. He, X. Zhang, S. Ren and J. Sun, *IEEE International Conference on Computer Vision*, 2015, 1026–1034.

28 Y. LeCun, B. E. Boser, J. S. Denker, D. Henderson, R. E. Howard, W. E. Hubbard and L. D. Jackel, *NIPS (News Physiol. Sci.)*, 1990, 396–404.

29 A. G. Howard, M. Zhu, B. Chen, D. Kalenichenko, W. Wang, T. Weyand, M. Andreetto and H. Adam, 2017, arXiv preprint arXiv:1704.04861.

30 A. Paszke, S. Gross, F. Massa, A. Lerer, J. Bradbury, G. Chanan, T. Killeen, Z. Lin, N. Gimelshein and L. Antiga, *NIPS (News Physiol. Sci.)*, 2019, **32**.

31 M. Hodak, M. Gorkovenko and A. Dholakia, Towards power efficiency in deep learning on data center hardware, in *2019 IEEE International Conference on Big Data (Big Data)*, IEEE, 2019, pp. 1814–1820.

32 X. Glorot and Y. Bengio, *ICAIS*, 2010.

33 D. P. Kingma and J. Ba, 2014, arXiv preprint arXiv:1412.6980.

34 R. Caruana, S. Lawrence and C. L. Giles, *NIPS (News Physiol. Sci.)*, 2001, 402–408.

35 D. A. Reynolds, *Encyclopedia of Biometrics*, 2009, p. 741.

36 W. M. Mendenhall and T. L. Sincich, *Statistics for Engineering and the Sciences*, CRC Press, 2016.

37 A. Corduneanu and C. M. Bishop, *ICAIS*, 2001.

38 D. A. Forsyth and J. Ponce, *Computer vision: a modern approach*, Pearson, 2012.